OPEN

NPG Asia Materials (2016) 8, e242; doi:10.1038/am.2016.3
www.nature.com/am

ORIGINAL ARTICLE

Ferroelectric polarization switching with a remarkably high activation energy in orthorhombic $GaFeO_3$ thin films

Seungwoo Song[1], Hyun Myung Jang[1], Nam-Suk Lee[2], Jong Y Son[3], Rajeev Gupta[4], Ashish Garg[5], Jirawit Ratanapreechachai[6] and James F Scott[7]

Orthorhombic $GaFeO_3$ (*o*-GFO) with the polar $Pna2_1$ space group is a prominent ferrite owing to its piezoelectricity and ferrimagnetism, coupled with magnetoelectric effects. Herein, we demonstrate large ferroelectric remanent polarization in undoped *o*-GFO thin films by adopting either a hexagonal strontium titanate (STO) or a cubic yttrium-stabilized zirconia (YSZ) substrate. The polarization-electric-field hysteresis curves of the polar c-axis-grown *o*-GFO film on a $SrRuO_3$/STO substrate show the net switching polarization of ~ 35 $\mu C\,cm^{-2}$ with an unusually high coercive field (E_c) of $\pm$ 1400 $kV\,cm^{-1}$ at room temperature. The positive-up and negative-down measurement also demonstrates the switching polarization of ~ 26 $\mu C\,cm^{-2}$. The activation energy for the polarization switching, as obtained by density-functional theory calculations, is remarkably high, 1.05 eV per formula unit. We have theoretically shown that this high value accounts for the extraordinary high E_c and the stability of the polar $Pna2_1$ phase over a wide range of temperatures up to 1368 K.
NPG Asia Materials (2016) **8,** e242; doi:10.1038/am.2016.3; published online 26 February 2016

INTRODUCTION

Multiferroics are an interesting group of materials that simultaneously exhibit ferroelectricity and magnetic ordering with coupled electric, magnetic and structural orders. Multiferroic materials with a pronounced degree of magnetoelectric (ME) coupling at room temperature are of great scientific and technological importance for use in various types of electronic devices that include sensors, actuators and electric-field-controllable magnetic memories.[1–3] Among all known multiferroics, $BiFeO_3$ is most extensively studied because of its large room-temperature-spontaneous polarization with improved magnetic properties in epitaxially strained thin-film forms.[4–7]

Polar orthorhombic $GaFeO_3$ (*o*-GFO) is another prominent multiferroic oxide by virtue of its room-temperature piezoelectricity (possibly ferroelectricity as well), near-room-temperature ferrimagnetism and pronounced low-temperature ME effects. Since a linear ME effect was first reported in the 1960s by Rado,[8] magnetization-induced second-harmonic generation,[9] the optical ME effect[10] and other interesting phenomena[11–22] continue to renew our research attention to this system. GFO crystallizes into the polar orthorhombic $Pna2_1$ (equivalently, $Pc2_1n$) space group with a ferrimagnetically ordered spin structure. The four Fe^{3+} ions in a unit cell are antiferromagnetically coupled along the a axis in the $Pna2_1$ setting. However, the intermixed Fe^{3+} ions occupying the Ga sites (in other words, different Fe occupations at the Fe1 and Fe2 sites) can lead to a ferromagnetic order with Fe^{3+} ions at the Fe sites, which gives rise to ferrimagnetic ordering at a temperature of ~ 230 K.[11,12]

In contrast to ferrimagnetic ordering and low-temperature ME effects,[11] much less is known on the ferroelectricity of *o*-GFO. In principle, *o*-GFO should exhibit ferroelectricity up to high temperatures as (or because) the polar $Pna2_1$ phase (with the corresponding point group of 2 mm or *C2v* in Schönflies notation) remains stable up to at least 1368 K.[22] According to Stoeffler,[20,23] the computed *ab initio* polarization value of the undoped *o*-GFO is as high as 25 $\mu C\,cm^{-2}$. In spite of these predictions, however, there has been no experimental demonstration of room-temperature ferroelectric polarization switching with a polarization value compatible with the *ab initio* predictions. Several groups have studied the *P*–*E* (polarization–electric field) response of GFO ferroelectrics, mostly using thin-film forms.[13–16] However, all of these studies revealed that the remanent polarization (P_r) of GFO is $<0.5\,\mu C\,cm^{-2}$ with an

[1]Division of Advanced Materials Science (AMS) and Department of Materials Science and Engineering, Pohang University of Science and Technology (POSTECH), Pohang, Republic of Korea; [2]National Institute for Nanomaterials Technology, Pohang University of Science and Technology (POSTECH), Pohang, Republic of Korea; [3]Department of Applied Physics, College of Applied Science, Kyung Hee University, Giheung-Gu, Republic of Korea; [4]Department of Physics and Materials Science Programme, Indian Institute of Technology (IIT), Kanpur, India; [5]Department of Materials Science and Engineering, Indian Institute of Technology (IIT), Kanpur, India; [6]Cavendish Laboratory, Department of Physics, University of Cambridge, Cambridge, UK and [7]School of Chemistry and Physics, St Andrews University, Scotland, UK
Correspondence: Professor HM Jang, Division of Advanced Materials Science (AMS) and Department of Materials Science and Engineering, Pohang University of Science and Technology (POSTECH), 77 Cheongam-Ro. Nam-Gu, Pohang 790-784, Republic of Korea.
E-mail: hmjang@postech.ac.kr
or Professor JF Scott, School of Chemistry and Physics, St Andrews, Scotland KY16 9ST, UK.
E-mail: jfs4@st-andrews.ac.uk
Received 22 June 2015; revised 17 November 2015; accepted 17 December 2015

unrealistically small value of the coercive field ($E_c \leqslant 5\ kV\ cm^{-1}$) as well. More recently, Oh *et al.*[17] reported the epitaxial growth of *o*-GFO film on an $SrRuO_3$ (111)/$SrTiO_3$ (111) substrate with a remarkably enhanced E_c of ~150 kV cm^{-1}. However, their P_r value still remains at ~0.05 μC cm^{-2}. Moreover, Mukherjee *et al.*[18] recently reported room-temperature ferroelectricity of an *o*-GFO thin film grown on a indium tin oxide (ITO) (001)/yttrium-stabilized zirconia (YSZ) (001) substrate based on their observation of a 180° phase shift in the piezoresponse. However, the 180° phase shift (or switching of the piezoelectric phase) does not necessarily indicate ferroelectric polarization switching across the barrier of a double-well potential.

To date, the only unequivocal experimental demonstration of reversible polarization switching in *o*-GFO thin films was made by Thomasson *et al.*[19] According to their study, the 2% Mg-doped GFO film exhibits a well-saturated *P–E* switching curve with a negligible tendency of the non-switching polarization.[19] However, the measured P_r value is as small as 0.2 μC cm^{-2},[19] which is <1% of the predicted P_r value (~25 μC cm^{-2}) of the undoped GFO. Moreover, this system is not a stoichiometric *o*-GFO (i.e., not an orthoferrite with Ga:Fe = 0.6:1.4) in addition to 2% Mg doping.[19] Thus, all reported P_r values of *o*-GFO are in the range of 0.05–0.5 μC cm^{-2}, which is unacceptably small to be compatible with the *ab initio* polarization of 25 μC cm^{-2}.[20,23]

In this article, we have clarified a puzzling discrepancy between the observed P_r value ($\leqslant$0.5 μC cm^{-2}) and the *ab initio* prediction (25 μC cm^{-2}) and unequivocally demonstrated ferroelectric polarization switching with a net switching polarization value of ~30 μC cm^{-2} by using *o*-GFO thin films preferentially grown along the polar c axis in $Pna2_1$ setting (b axis in $Pc2_1n$ setting). In the present study, we adopt either a hexagonal or a cubic substrate to demonstrate the room-temperature polarization switching: (i) a $SrRuO_3$ (SRO) (111)-buffered hexagonal strontium titanate (STO) (111) substrate and (ii) an ITO (001)-buffered cubic YSZ (001) substrate.

MATERIALS AND METHODS

Experimental methods

The *o*-GFO film and the SRO bottom-electrode layer were grown on a Ti^{4+}-single-terminated STO (111) substrate by pulsed laser deposition with a KrF excimer laser (λ = 248 nm) operated at 3 and 10 Hz, respectively. GFO films were deposited at 800 °C in an oxygen ambient atmosphere (200 mTorr) with a fluence of 1 J cm^{-2} focusing on a stoichiometrically sintered *o*-GFO target while 30-nm-thin SRO bottom-electrode layers were grown at 680 °C in a 100 mTorr oxygen atmosphere with a fluence of 2 J cm^{-2}. After the deposition, the SRO layer was cooled to room temperature under the same oxygen pressure used in the *o*-GFO film deposition. We observed the thickness fringes of SRO (222) around the two-theta (2θ) value of STO (222), which strongly indicates an epitaxial growth of the SRO bottom-electrode layer. The thickness of this SRO layer (30 nm) was also determined from the positions of the interference fringes (see Supplementary Information for details). The *o*-GFO film and the ITO bottom-electrode layer were grown on a cubic YSZ (001) substrate by pulsed laser deposition with operating ac frequencies of

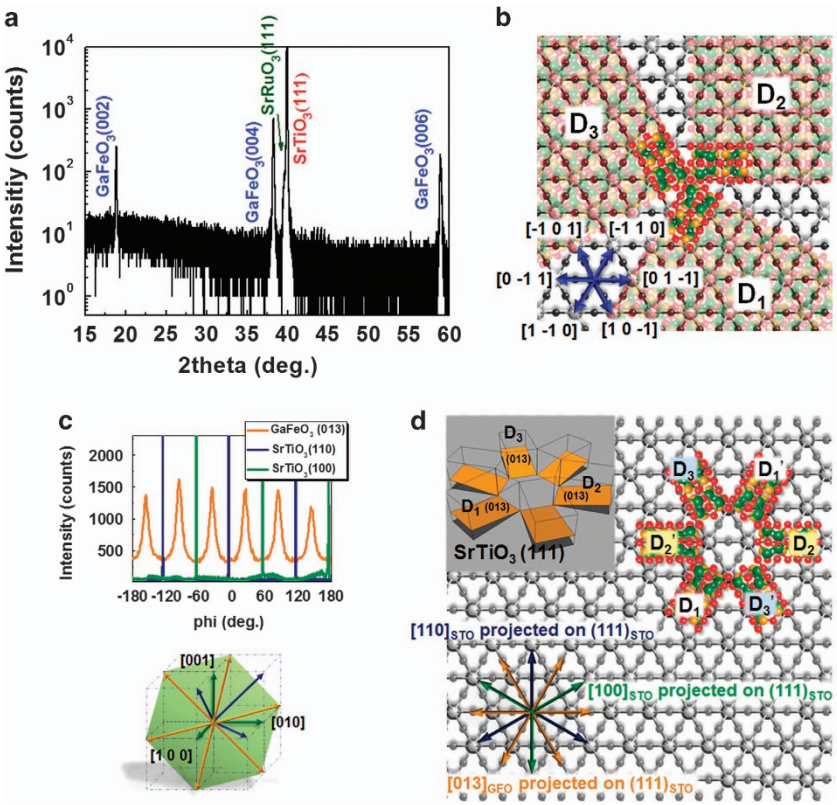

Figure 1 X-ray diffraction (XRD) data and in-plane domain orientations. (**a**) $\theta-2\theta$ XRD pattern of the [001]-oriented 200-nm-thin $GaFeO_3$ (GFO) thin film grown on a $SrRuO_3$ (SRO) (111)-buffered hexagonal strontium titanate (STO) (111) substrate. (**b**) Schematic representation of the most probable domain configuration for the polar c-axis-oriented GFO film grown on an STO (111) substrate. Blue bidirectional arrows refer to in-plane orientation of the STO (111) substrate. (**c**) In-plane XRD φ-scan spectra of the polar c-axis grown GFO film, as obtained by maintaining the Bragg angle at (013) for orthorhombic $GaFeO_3$ (*o*-GFO) film (orange line) and at (110) and (100) for STO (blue and green lines, respectively). A schematic diagram presented below the φ-scan spectra denotes the projected normal vectors of (013) for GFO on STO (111) and projected normal vectors of (110) and (100) STO on STO (111). (**d**) A schematic domain configuration of the polar c-axis-oriented GFO film grown on an STO (111) substrate showing six in-plane domain orientations with three distinct crystallographic variants. Three different types of the projected normal vectors are shown in the lower corner.

3 and 10 Hz, respectively. The deposition conditions of the *o*-GFO film are similar to those of the o-GFO film on an SRO/STO (111) substrate, except for the deposition temperature (700 °C). On the other hand, 30-nm-thin ITO bottom-electrode layers were grown at 600 °C in a 20 mTorr oxygen atmosphere with a fluence of 1.5 J cm^{-2}.

Analysis of the domain orientation and phase formation in the films was performed by using a high-resolution x-ray diffractometer (D8 discover; Bruker, Billerica, MA, USA) under Cu Kα radiation. The domain structures were investigated in detail by using high-resolution transmission electron microscopy (JEM-2100F with a probe CS corrector; JEOL, Tokyo, Japan). *Z*-contrast high-angle annular dark-field scanning transmission electron microscopy (STEM) image and selected-area electron diffraction experiments were carried out under 200-kV acceleration voltage.

For dielectric–ferroelectric measurements of the c-axis-grown *o*-GFO film, a Pt top electrode with a diameter of 100 μm was deposited using a dc sputtering system. Current and voltage (*I*–*V*) curves were recorded using a Keithley 2400 source meter (Keithley, Cleveland, OH, USA). Polarization–electric field hysteresis loops (*P*–*E* curves) and positive-up and negative-down (PUND) pulse sequences were measured using a precision LC ferroelectric tester (Radiant Technologies, Albuquerque, NM, USA). A commercial atomic force microscope (DC-EFM in XE-100; Park Systems, Suwon, Korea) was used for vertical piezoelectric force microscopy (vPFM) study to map the piezoelectric properties of thin films. A Pt/Ir-coated tip was used for probing the signals. The input modulation voltage V_{ac} (with an amplitude in the range of 0.1–2 V and an ac frequency of 15 kHz) was applied between the conductive tip and the bottom electrode using a function generator. The resulting oscillations of the cantilever were read out with a lock-in amplifier. The magnetic properties were measured by superconducting quantum interference device magnetometry (MPMS; Quantum Design, San Diego, CA, USA) from 10 to 300 K under various applied magnetic fields.

Computational methods

We have performed DFT calculations of *o*-GFO based on the generalized gradient approximation[24] and generalized gradient approximation+U methods[25] implemented with projector augmented-wave pseudopotential[26,27] using the *Vienna ab initio Simulation* Package.[28] All DFT calculations were performed by adopting (i) an 11×6×6 Monkhorst–Pack ***k***-point mesh[29] centered at the *Γ*-point, (ii) 650-eV plane-wave cutoff energy and (iii) the tetrahedron method with Blöchl corrections for the Brillouin-zone integrations.[30] The structural optimizations were performed for the 40-atom cell that corresponds to an orthorhombic unit cell consisting of eight formula units. The ions were relaxed until the Hellmann–Feynmann forces on them were <0.01 eV $Å^{-1}$. A Hubbard U_{eff} of 4 eV and an intra-atomic exchange parameter (*J*) of 0.89 eV for the Fe 3*d* orbital were chosen based on the previous work.[20]

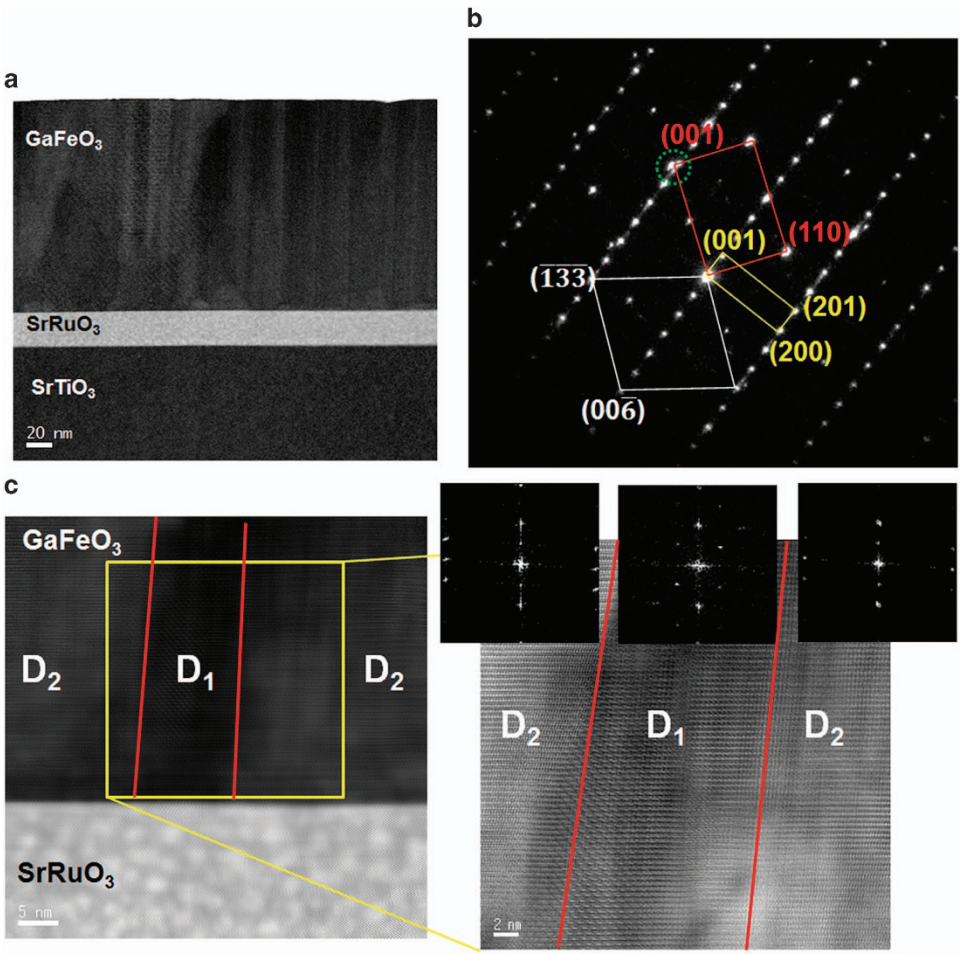

Figure 2 Scanning transmission electron microscopy (STEM) images of the polar c-axis-oriented $GaFeO_3$ (GFO) film. (**a**) A cross-sectional high-angle annular dark-field STEM (HADDF-STEM) image of the polar c-axis-oriented GFO film grown on a $SrRuO_3$ (SRO) (111)-buffered hexagonal strontium titanate (STO) (111) substrate. (**b**) A selected-area electron diffraction (SAED) pattern confirming the in-plane orientation between the GFO film and the STO substrate. The diffraction pattern is indexed by considering the superposition of the diffracted peaks along the zone axes $[3\bar{1}0]$ and [010] of the GFO and the zone axis $[1\bar{1}0]$ of the STO. (**c**) An HAADF STEM image of the interfacial region between the polar c-axis-oriented GFO film and the SRO electrode layer. The area surrounded by a yellow rectangle is magnified in the right-hand side to clearly visualize the structural domain boundary. Three fast Fourier-transformed images are also shown in the upper region of the magnified STEM image.

RESULTS

In-plane domain orientation of the polar c-axis-grown film

To fabricate the polar c-axis-grown GFO film with a simpler domain configuration, we have carefully chosen a hexagonal STO (111) substrate as an alternative to a cubic YSZ (001) substrate. To implement this, we adopt an SRO (111) bottom electrode by considering its compatibility with the STO substrate and fatigue and imprinting resistance.[31,32] This scheme of the *o*-GFO film growth on a hexagonal substrate enables us to achieve a substantial simplification in the domain configuration, from 12 orientations (on a cubic YSZ (001) substrate[18]) to 6 in-plane orientations. Figure 1a shows that the [001]-oriented GFO thin film is preferentially grown on an SRO (111)-buffered STO(111) substrate. The calculated c-axis parameter using this $\theta-2\theta$ XRD pattern is 9.3996 Å, which essentially coincides with the bulk c-axis parameter.[13] This suggests that the present GFO film is fully relaxed along the growth direction. For the [001]-oriented film grown on an STO(111), the most probable domain orientation that minimizes the in-plane lattice mismatch is represented by three in-plane domain configurations (D_1, D_2 and D_3), as schematically depicted in Figure 1b.

To examine the validity of the proposed domain configuration, we have measured the in-plane XRD phi(φ)-scan, and the result is presented in Figure 1c. These φ-scan spectra were obtained by maintaining the Bragg angle at (013) for the *o*-GFO film (orange line) and at (110) and (100) for the STO (blue and green lines, respectively). In the case of the *o*-GFO (013), six peaks appear (orange color), each of which is separated from the two neighboring GFO (013) peaks by 60°. However, as shown in Figure 1c, these six (013) peaks are separated from the STO (110) and (100) peaks by 30°. These two observations clearly indicate that the GFO (013) has six in-plane orientations with a successive tilting angle of 60° when projected onto an STO (111) surface, and each of these six in-plane orientations is rotated by 30° from the STO (111) projection of the STO (110) and (100) vectors. The domain configuration depicted in Figure 1d satisfies all of these orientation relationships. The six projected normal vectors of the GFO (013) are shown in orange in the lower corner of Figure 1d. Thus, the *o*-GFO film grown on the STO (111) surface is

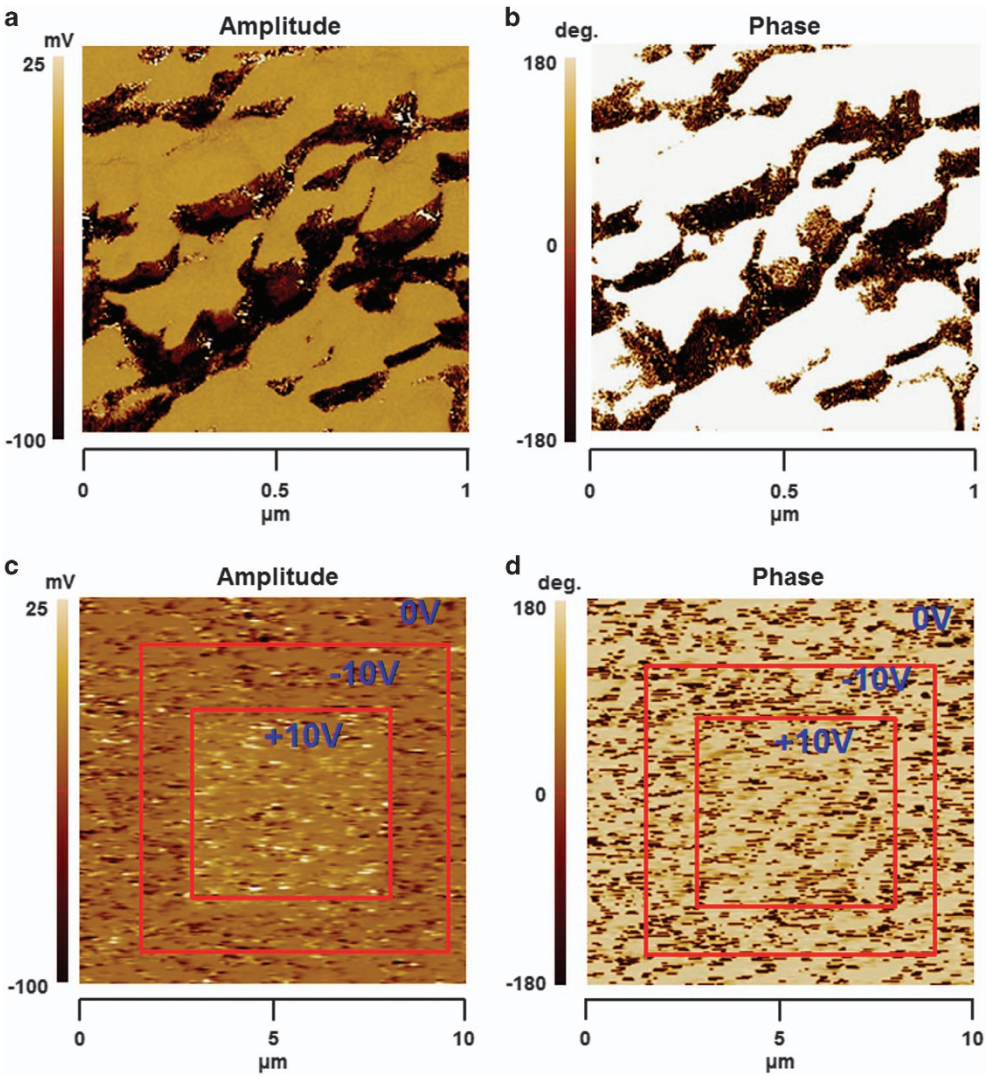

Figure 3 Vertical-mode piezoelectric force microscopy (PFM) images of the polar c-axis-oriented GFO film. The $GaFeO_3$ (GFO) film was grown on a $SrRuO_3$ (SRO) (111)-buffered strontium titanate (STO) (111) substrate. PFM (**a**) amplitude and (**b**) phase-contrast images of the GFO film acquired over an area of 1 μm × 1 μm. PFM (**c**) amplitude and (**d**) phase-contrast images of the two concentric square regions obtained after applying an alternative dc voltage from +10 V to − 10 V and subsequently turning off these dc voltages.

characterized by three distinct crystallographic variants, D_1, D_2 and D_3, and is represented by a total of six in-plane orientations—namely, $D_1, D_1^{'}, D_2, D_2^{'}$ and $D_3, D_3^{'}$, where Dn and $D_n^{'}$ are facing each other with the same crystallographic variant. This domain configuration (Figure 1d) agrees well with our previous proposition deduced from minimizing the lattice mismatch (Figure 1b). The result of our structural analysis is very similar to the previous result on ε-Fe_2O_3, which is isostructural with the *o*-GFO grown on an STO (111).[33] In contrast, the *o*-GFO film grown on an ITO/YSZ (001) substrate is characterized by a total of 12 in-plane orientations with a successive in-plane tilting angle of 30° (see Supplementary Information for details).

However, there exists a considerable degree of lattice mismatch (Δ), although the (001)-oriented GFO film possesses six in-plane orientations to reduce the lattice mismatch between the film and substrate. According to our estimate, $\Delta a = 5.8654\%$ ($a_{GFO} = 5.0806$ Å, $\sqrt{2}a_{STO}\cos(30^o)$) and $\Delta b = 5.3388\%$ ($b_{GFO} = 8.7510$ Å, $3\sqrt{2}a_{STO}\cos(60^o)$).[13,30] This indicates that the *o*-GFO film is unable to show cube-on-cube type growth on the unit-cell basis. However, if the *o*-GFO film growth is preceded by the formation and deposition of a supercell with the dimensions of $16a_{GFO} \times 18b_{GFO}$, the lattice mismatch between the GFO layer and the substrate surface can be effectively removed (with $\Delta a = 0.01\%$, $\Delta b = 0.08\%$). We will examine this proposition by looking into scanning transmission electron microscopy (STEM) images.

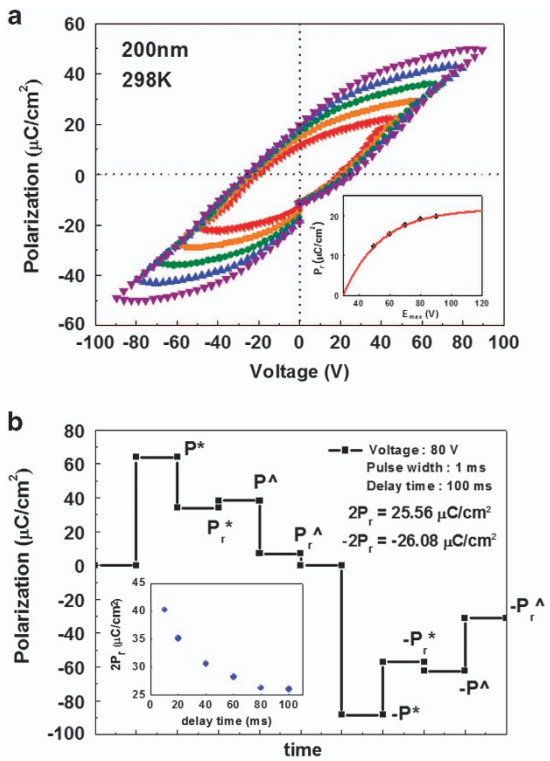

Figure 4 Ferroelectric responses of the $GaFeO_3$ (GFO) film grown on a hexagonal strontium titanate (STO) substrate. (**a**) *P*–*E* (polarization–electric field) curves of the Pt/GFO (001)/$SrRuO_3$ (SRO) (111) film capacitor grown on an STO (111) showing ferroelectric switching behavior with a high coercive field (E_c) of $\pm 1400\,kV\,cm^{-1}$ at 298 K. (**b**) Positive-up and negative-down (PUND) test result of the polar c-axis-oriented 200-nm-thin GFO film capacitor grown on an SRO (111)/STO (111) obtained using a pulse delay time of 100 ms.

A bright-field STEM image is shown in Figure 2a for the cross-section of the [001]-oriented GFO film grown on an SRO(111)-buffered STO(111) substrate. According to this cross-sectional image, the thicknesses of the GFO layer and the SRO electrode are 200 and 30 nm, respectively. The selected-area electron diffraction pattern shown in Figure 2b is indexed by considering the superposition of the diffracted peaks along the zone axes [010] and $[3\bar{1}0]$ of the GFO and the peaks along the STO $[1\bar{1}0]$ zone axis (red rectangle) used as the standard. The diffracted peaks along the GFO [010] zone axis (yellow rectangle) correspond to the D_1 domain configuration (Figure 1). In contrast, the peaks along the GFO $[3\bar{1}0]$ zone axis (white rhombus) correspond to the D_2 domain configuration. The selected-area electron diffraction patterns also indicate epitaxial growth of the GFO film with the polar axis along the growth direction. One can notice two separated peaks by carefully examining the area encircled by green dots. This demonstrates that the GFO film is fully relaxed rather than epitaxially strained.

High-resolution high-angle annular dark-field STEM images clearly show structural domain boundaries that are formed by distinct in-plane orientations. A high-angle annular dark-field STEM image of the area surrounded by a yellow rectangle is magnified and presented on the right-hand side of Figure 2c to visualize clearly the structural domain boundary. The three fast Fourier-transformed images (upper regions of the magnified STEM image) indicate that the in-plane orientation of the central domain is different from those of the two neighboring domains. Figure 2c indicates that the width of the central domain is ~8 nm, which nearly coincides with the a-axis dimension of the supercell proposed previously ($16a_{GFO} \times 18b_{GFO}$). Thus, the central domain in Figure 2c represents the D_1 domain configuration, as depicted in Figure 1.

PFM images of the polar c-axis-grown film

vPFM is a suitable method for measuring ferroelectricity or piezoelectricity for a small local region. In Figures 3a and b, we present vPFM amplitude and phase images, respectively, acquired over an area of 1 μm × 1 μm (or simply 1 μm^2). The phase-contrast image shown in Figure 3b can be interpreted as the existence of ferroelectric domains with two antiparallel polarizations. However, this interpretation would be false if these domains were not maintained at a particular polarization state (i.e., remain in either up or down state) after turning off the bias *E*-field, which had been used for the polarization switching. To resolve clearly this critical issue, we have chosen a particular region of the *o*-GFO film and applied an alternative dc voltage from +10 V to −10 V. Thus, the corresponding *E*-field is $\pm 500\,kV\,cm^{-1}$. The two applied voltages and the corresponding regions are marked in Figures 3c and dfor the amplitude and phase-contrast images, respectively. The two lower-resolution vPFM images (10 μm × 10 μm) shown in Figures 3c and d were taken immediately after turning off these dc voltages. Figure 3d clearly indicates that the 180° phase-shifted domains by the bias *E*-field return to the initial unshifted state as soon as the bias *E*-field is turned off. Thus, the present vPFM results do not show any evidence of ferroelectricity with a nonzero remanent polarization up to a bias *E*-field of $\pm 500\,kV\,cm^{-1}$.

Ferroelectric polarization switching of the polar c-axis-grown films

Having failed to obtain clear evidence of the ferroelectricity up to $\pm 500\,kV\,cm^{-1}$, we have carried out *P*–*E* hysteresis measurement by applying much stronger *E*-fields. This has been performed because our optimally processed [001]-oriented GFO/SRO/STO (111) film capacitors are characterized by *I*–*V* current densities as low as $\sim 10^{-6}\,A\,cm^{-2}$ even at $\pm 500\,kV\,cm^{-1}$ (i.e., at ±10 V; see

Supplementary Information for details). This low leakage current is a remarkable improvement over those of other reported GFO films. For instance, the current density of the previously reported GFO/SRO/STO (111) film capacitor (with 0% MgO doping) is in the order of a few amps per square centimeter for the same thickness of 200 nm (i.e., at $\pm 500\,kV\,cm^{-1}$).[34] Thus, our film capacitor processed by the optimized layer-by-layer growth of SRO shows a remarkable 10^6-fold improvement in the leakage current density (10^{-6} vs 10^0). Similarly, the reported current density of the GFO/Pt/YSZ (111) film capacitor at 300 K is as high as $1.4\times10^{-2}\,A\,cm^{-2}$ (as estimated using 300 μm as the diameter of the top electrode) for the same thickness of 200 nm (i.e., at $\pm 500\,kV\,cm^{-1}$).[35] Again, our film capacitor shows a remarkable ~10^4-fold improvement in the leakage current density.

The Pt/*o*-GFO (001)/SRO (111) film capacitor grown on an STO (111) shows ferroelectric switching behavior with a remarkably high coercive field (E_c) of $\pm 1400\,kV\,cm^{-1}$ at room temperature (Figure 4a). Thus, the E_{max} value used in the PFM measurements is only 1/3 of the minimum electric field needed for polarization switching (E_c). Thus, ferroelectric polarization switching cannot be attained by PFM techniques (with E_{max} of ±10 V), although a 180° phase shift of the piezoresponse is readily observed. As shown in the inset of Figure 4a, P_r tends to reach its saturated value with increasing E_{max}. This type of saturation tendency in P_r is also observed with increasing E_c (Supplementary Figure S8). Thus, the net switching polarization ($2P_r$) estimated from Figure 4a is ~35 $\mu C\,cm^{-2}$, which is much larger than the previously reported values of $2P_r$ (between 0.1 and 1.0 $\mu C\,cm^{-2}$).[14–16]

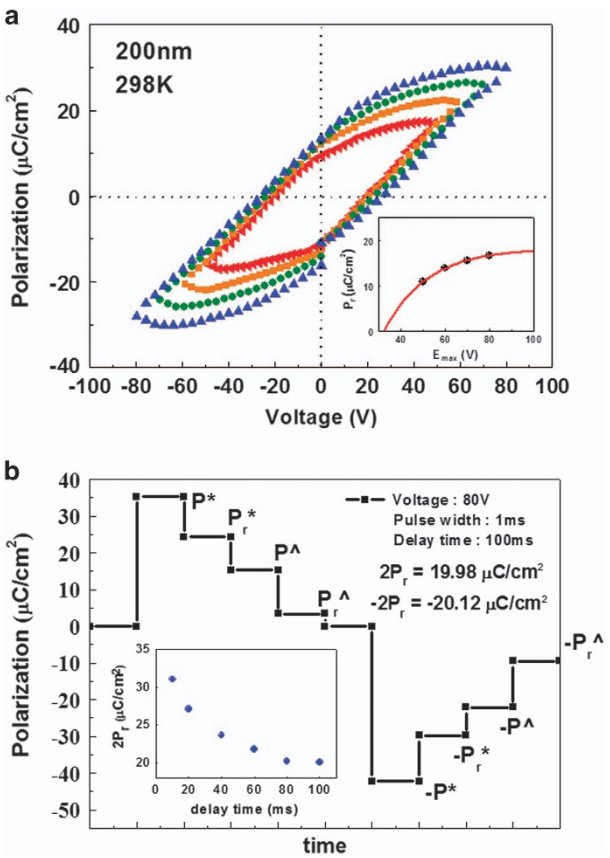

Figure 5 Ferroelectric responses of the $GaFeO_3$ (GFO) film grown on a cubic yttrium-stabilized zirconia (YSZ) substrate. (**a**) *P–E* (polarization–electric field) curves of the Pt/GFO (001)/indium tin oxide (ITO) (001) film capacitor grown on a YSZ (001). The coercive field (E_c) deduced from these curves is $\pm 1100\,kV\,cm^{-1}$ at 298 K. (**b**) Positive-up and negative-down (PUND) test result of the polar c-axis-oriented 200-nm-thin GFO film capacitor grown on an ITO (001)/YSZ (001).

A more reliable value of the switching polarization can be obtained by using PUND (positive-up and negative-down) pulse test. Figure 4b presents the PUND result of the 200-nm-thin GFO film capacitor obtained using the pulse delay time of 100 ms. We have found that the switching polarization decreases with increasing delay time and reaches a saturated value for pulse delay times longer than ~80 ms. The net switching polarization ($2P_r$) is evaluated using the following relation: $2P_r = (\pm P^*) - (\pm P^{\Lambda})$ The $2P_r$ value obtained from Figure 4b is ~26 $\mu C\,cm^{-2}$. Comparing this value with the $2P_r$ value obtained from Figure 4a, one can conclude that the *P–E* curves overestimate the $2P_r$ value substantially. This suggests that the ac frequency of 1 kHz used in the *P–E* measurement is not sufficiently high to eliminate completely the responses of mobile space charges, which tend to be significant at lower ac frequencies.

To examine the universality of the present finding of a large $2P_r$, we have also examined the polarization switching characteristics of the polar c-axis-oriented GFO film grown on a conducting ITO-buffered cubic YSZ (001) substrate. As shown in Figure 5a, the GFO film (with the same 200-nm thickness) grown on an ITO (001)/YSZ (001) substrate is characterized by the net switching polarization of ~30 $\mu C\,cm^{-2}$ at 298 K. Compared with the Pt/GFO/SRO/STO (111) capacitor (Figure 4a), the *P–E* curves of the Pt/GFO/ITO/YSZ (001) capacitor (Figure 5a) tend to have a more noticeable electrical leakage problem. The *I–V* current density data support this tendency of electrical leakage in the Pt/GFO/ITO/YSZ (001) capacitor (see Supplementary Figure S3b of Supplementary Information). The PUND result shown in Figure 5b also demonstrates that the Pt/GFO/ITO/YSZ (001) capacitor (with a 200-nm-thin GFO layer) is ferroelectric with net switching polarization of ~20 $\mu C\,cm^{-2}$ at 298 K.

Compared with the $2P_r$ of the Pt/GFO/SRO/STO (111) capacitor, the $2P_r$ of the Pt/GFO/ITO/YSZ (001) capacitor is thus substantially reduced: ~35 vs ~30 $\mu C\,cm^{-2}$ according to their *P–E* results. As stated previously, the c-axis-grown *o*-GFO film on an ITO/YSZ (001) substrate is characterized by the six crystallographic variants with a total of 12 in-plane orientations with a successive in-plane tilting angle of 30°, in spite of slight lattice mismatch between the GFO film and the YSZ substrate (see Supplementary Information for details). The reduced $2P_r$ value can possibly be correlated with this increase in the crystallographic variants (i.e., the degree of complexity in the domain configuration) upon replacing the SRO/STO (111) substrate with the ITO/YSZ (001) substrate. However, further in-depth studies should be made before clearly resolving the origin of the substrate-dependent $2P_r$.

DISCUSSION

For an in-depth understanding of the atomic-scale origin of the observed polarization switching, we have calculated the DFT polarization of the polar $Pna2_1$ phase of *o*-GFO using the Berry-phase method.[36,37] To obtain a correct evaluation of the ferroelectric polarization, a centrosymmetric prototypic phase of GFO should be identified first. To accomplish this, we have used the pseudocode of the Bilbao crystallographic server,[38] which allows one to determine the nearest supergroup structure for an input arbitrary structure based on lattice dynamics calculations. In the present case, four centrosymmetric supergroup structures are examined: *Pnna*, *Pccn*, *Pbcn* and *Pnma*. Among these four, the nearest reference structure, in terms

of the total displacement of all atoms, is the *Pnna* phase, which is consistent with the previously reported result.[20] The optimized lattice parameters of the ferroelectric *Pna*2_1 and prototypic *Pnna* phases were subsequently obtained by calculating the Kohn–Sham (K–S) energy as a function of the unit-cell volume and finding its minimum that corresponds to the ground state K–S energy in the absence of any external pressure. The optimized lattice parameters are (i) $a=5.1647$ Å, $b=8.8197$ Å and $c=9.5079$ Å for the *Pna*2_1 structure, and (ii) $a=5.2672$ Å, $b=8.9193$ Å and $c=9.5684$ Å for the *Pnna* structure. The optimized structures of the *Pnna* and *Pna*2_1 phases of *o*-GFO are depicted in Figure 6a.

According to group theoretical analysis,[39,40] there exists only one conceivable transition path that connects the prototypic *Pnna* phase to the ferroelectric *Pna*2_1 phase. We have decomposed the atomic displacements that relate the nonpolar *Pnna* phase to the polar *Pna*2_1 phase into the symmetry-adapted mode of the prototypic phase. The resulting symmetry-adapted mode is exclusively given by Γ_4^- Thus, the *Pnna*-to-*Pna*2_1 phase transition should be mediated by freezing in the zone-center Γ_4^- polar phonon. Let us define the displacement amplitude of the polar Γ_4^- phonon as $Q_{\Gamma_4^-}$. In Figure 6b, the K–S energy and Berry-phase polarization are plotted as functions of the mode amplitude $Q_{\Gamma_4^-}$.[41] Here, the polarization (lower panel of Figure 6b) is given by the product of $Q_{\Gamma_4^-}$ and the Born effective charge tensor. As shown in Figure 6b, the computed K–S energy exhibits a double-well-type potential, which demonstrates the relative stability of the ferroelectric *Pna*2_1 phase over the prototypic nonpolar *Pnna* phase with the energy difference of 1.05 eV per formula unit (f.u.). Herein, the equilibrium ferroelectric polarization of the *Pna*2_1 phase is given by the computed polarization values (lower panel) at the two K–S energy minima—namely, ± 25.67 μC cm^{-2}—which correspond to $Q_{\Gamma_4^-}$ of ± 1, respectively. Because polarization switching is expected to occur along the *Pna*2_1-to-*Pnna* phase-transition path—that is, Γ_4^-—the activation free energy of the polarization switching between the double wells can be obtained from Figure 6b, which is ~1.05 eV per f.u. This value lies within the two extreme *ab initio* values (0.52 and 1.30 eV per f.u.) previously obtained by Stoeffler[20] using ABINIT and FLAPW/FLEUR codes. The activation barrier of 1.05 eV per f.u. is ~2.5 times larger than that of $BiFeO_3$, the most extensively studied multiferroic, and 20 times larger than that of $Pb(Zr,Ti)O_3$, the most widely used displacive ferroelectric.[42] This unusually high activation barrier indicates that the polar *Pna*2_1 phase in *o*-GFO is very stable against thermally activated random dipole switching across the centrosymmetric *Pnna* barrier.

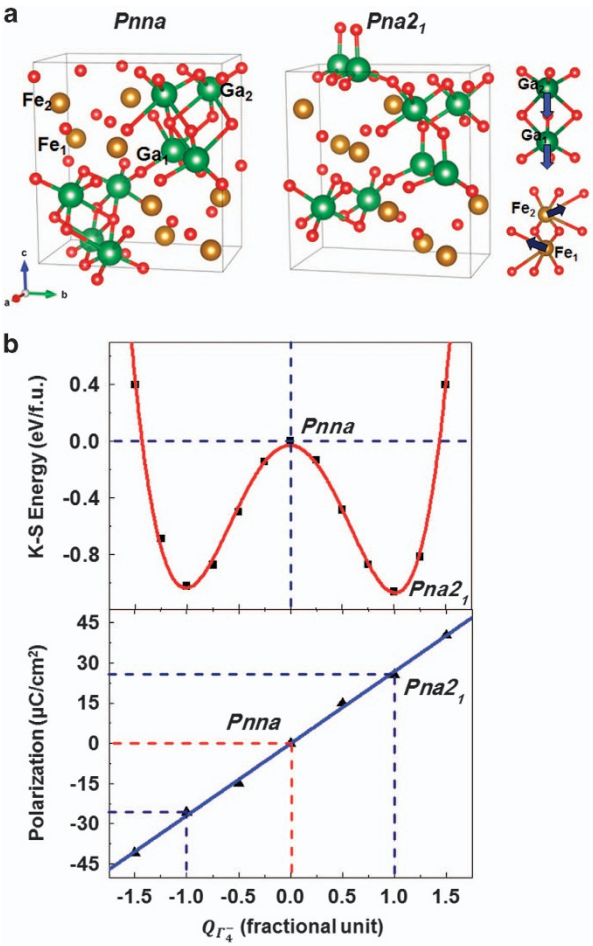

Figure 6 Crystal structures and the associated ferroelectric double-well potential. (**a**) Optimized unit-cell crystal structures of prototypic *Pnna* and polar *Pna*2_1 phases of orthorhombic $GaFeO_3$ (*o*-GFO) obtained after structurally relaxing the computed Kohn–Sham energy as a function of the unit-cell volume. Eigenvectors of the Γ_4^- phonons at Ga and Fe ions are shown in the right-hand side using blue arrows. (**b**) The computed Kohn–Sham energy plotted as a function of the fractional amplitude $Q_{\Gamma_4^-}$. The reference state of $Q_{\Gamma_4^-}=0$ denotes the prototypic *Pnna* phase. In the lower panel, the computed polarization values are plotted as a function of $Q_{\Gamma_4^-}$.

We will then theoretically correlate the reported high ferroelectric transition temperature (>1368 K; Mishra *et al.*[22]) with this remarkably high activation free energy. According to the transition-state theory of rate processes,[43] the frequency (ν) of the polarization switching across the *Pnna* potential barrier can be written as

$$\nu = \frac{k_B T}{h} e^{-\Phi_o/k_B T}. \quad (1)$$

where Φ_0 is the barrier height of the polarization switching, which can be treated as the difference in the K–S energy between the *Pnna* and *Pna*2_1 phases (1.05 eV per f.u.). Strictly speaking, Equation (1) is valid for describing the dipole switching rate of order–disorder ferroelectrics. For sufficiently high temperatures near the phase transition point (T_c), however, Equation (1) is also applicable to the dipole switching rate of displacive ferroelectrics,[44] which include the present *Pna*2_1-to-*Pnna* transition. As temperature increases and approaches T_c, the dipole switching rate becomes so rapid that the mean residence time (τ_0) of the bound polarization in one of the two ferroelectric double wells becomes shorter than a certain critical time for the experimental observation. Under this condition, the net ferroelectric polarization effectively disappears because of the switching average of two opposite polarizations across the centrosymmetric barrier (*Pnna* state in the present case; Figure 6b). Let ν_0 be the frequency at which the net bound polarization first begins to disappear. In the vicinity of T_c, $\Phi_0 < k_B T$ for a fixed value of Φ_0. Under this condition, ν_0 can be approximated by the following expression:

$$\nu_o = \frac{1}{\tau_o} \approx \frac{k_B T_o}{h}\left(1 - \frac{\Phi_o}{k_B T_o}\right). \quad (2)$$

where T_0 denotes the temperature that corresponds to the critical switching frequency ν_0. Because T_c is expressed by $T_c = T_o + \epsilon$, where ϵ is a small positive number (including zero), T_c can be correlated with Φ_0 by the following relation for a fixed value of Φ_0:

$$T_c = \frac{(h\nu_o + \Phi_o)}{k_B} + \epsilon \approx \frac{(h\nu_o + \Phi_o)}{k_B}. \quad (3)$$

Equation (3) clearly indicates that T_c is linearly proportional to Φ_0. This explains the observed high T_c of *o*-GFO in terms of the unusually high activation energy barrier (Φ_0) as predicted by *ab initio* calculations.

Finally, we will correlate both the observed large polarization and the high coercive field (E_c) with the high activation energy barrier, Φ_0 by exploiting the phenomenological Landau theory. To accomplish this, let us write the elastic Gibbs free energy density (at a constant pressure or stress) of the polar $Pna2_1$ phase of *o*-GFO in terms of the polarization as a relevant order parameter (up to P^4-term):

$$\Delta G \equiv G_{Pna2_1} - G_{Pnna} = \frac{1}{2}\chi P^2 + \frac{1}{4}\xi P^4 \leq 0. \quad (4)$$

where $\xi > 0$ for the P^4 expansion and $\chi = (T - T_c)/C < 0$ for temperatures below T_c, where C and T_c denote the Curie–Weiss constant and Curie–Weiss temperature, respectively. Starting from Equation (4), one can derive the following expression of the equilibrium polarization (P_{eq}) in terms of the barrier height of the ferroelectric double-well potential (Φ_0; 1.05 eV as shown in Figure 6b):

$$P_{eq}^2 = 2\left(\frac{\Phi_o}{\xi}\right)^{1/2}. \quad (5)$$

Similarly, the following relation between the coercive field and the barrier height can be derived (detailed derivations are given in the Supplementary Information):

$$E_c = \frac{4\sqrt{3}}{9}\{|\chi|\Phi_o\}^{1/2}. \quad (6)$$

According to Equation (6), the coercive field is proportional to the square root of the barrier height (Φ_0). It is now clear that this high value of Φ_0 is responsible for both the observed large equilibrium polarization (Equation (5)) and the high coercive field (Equation (6)). Although the phenomenological Landau theory is strictly valid for a single-domain ferroelectric, the conclusions drawn above can be applied to the present polar *c*-axis grown *o*-GFO thin film, at least qualitatively.

CONCLUSIONS

We have clarified a puzzling discrepancy between the observed P_r values ($\leqslant 0.5\,\mu C\,cm^{-2}$) and the *ab initio* prediction and have unequivocally demonstrated ferroelectric polarization switching with net switching polarization ($2P_r$) of $\sim 30\,\mu C\,cm^{-2}$ by using the two distinct types of *o*-GFO thin films preferentially grown along the polar c-axis in $Pna2_1$ setting (b-axis in $Pc2_1n$ setting). The estimated activation energy for the polarization switching is ~ 1.05 eV per f.u. This high value accounts for the extraordinarily high coercive field ($> 1100\,kV\,cm^{-1}$) and the stability of the polar $Pna2_1$ phase over the centrosymmetric *Pnna* phase for a wide range of temperatures up to 1368 K.

CONFLICT OF INTEREST

The authors declare no conflict of interest.

ACKNOWLEDGEMENTS

This work was supported by the National Research Foundation (NRF) Grants funded by the Korea Government (MSIP) (Grant No. 2012R 1A1A2041628 and 2013R 1A2A2A01068274). The work at Cambridge was supported by the Engineering and Physical Sciences Research Council (EPSRC). AG and RG thank the Department of Science and Technology for the financial support (Grant No. SB/S3/ME/29/2013).

1 Scott, J. F. Multiferroic memories. *Nat. Mater.* **6**, 256 (2007).
2 Chu, Y., Martin, L. W., Holcomb, M. B. & Ramesh, R. Controlling magnetism with multiferroics. *Mater. Today* **10**, 16 (2007).
3 Spaldin, N. A. & Fiebig, M. The renaissance of magnetoelectric multiferroics. *Science* **309**, 391 (2005).
4 Wang, J., Neaton, J. B., Zheng, H., Nagarajan, V., Ogale, S. B., Liu, B., Viehland, D., Vaithyanathan, V., Schlom, D. G., Waghmare, U. V., Spaldin, N. A., Rabe, K. M., Wuttig, M. & Ramesh, R. Epitaxial $BiFeO_3$ multiferroic thin film heterostructures. *Science* **299**, 1719 (2003).
5 Zhao, T., Scholl, A., Zavaliche, F., Lee, K., Barry, M., Doran, A., Cruz, M. P., Chu, Y. H., Ederer, C., Spaldin, N. A., Das, R. R., Kim, D. M., Baek, S. H., Eom, C. B. & Ramesh, R. Electrical control of antiferromagnetic domains in multiferroic $BiFeO_3$ films at room temperature. *Nat. Mater.* **5**, 823 (2006).
6 Bibes, M. & Barthélémy, A. Multiferroics: towards a magnetoelectric memory. *Nat. Mater.* **7**, 425 (2008).
7 Catalan, G. & Scott, J. F. Physics and applications of bismuth ferrite. *Adv. Mater.* **21**, 2463 (2009).
8 Rado, G. T. Observation and possible mechanisms of magnetoelectric effects in a ferromagnet. *Phys. Rev. Lett.* **13**, 335 (1964).
9 Ogawa, Y., Kaneko, Y., He, J. P., Yu, X. Z., Arima, T. & Tokura, Y. Magnetization-induced second harmonic generation in a polar ferromagnet. *Phys. Rev. Lett.* **92**, 047401 (2004).
10 Jung, J. H., Matsubara, M., Arima, T., He, J. P., Kaneko, Y. & Tokura, Y. Optical magnetoelectric effect in the polar $GaFeO_3$ ferrimagnet. *Phys. Rev. Lett.* **93**, 037403 (2004).
11 Arima, T., Higashiyama, D., Kaneko, Y., He, J. P., Goto, T., Miyasaka, S., Kimura, T., Oikawa, K., Kamiyama, T., Kumai, R. & Tokura, Y. Structural and magnetoelectric properties of $Ga_{2-x}Fe_xO_3$ single crystal grown by a floating-zone method. *Phys. Rev. B* **70**, 064426 (2004).
12 Han, M. J., Ozaki, T. & Yu, J. Magnetic ordering and exchange interactions in multiferroic $GaFeO_3$. *Phys. Rev. B* **75**, 060404 (2007).
13 Trassin, M., Viart, N., Versini, G., Loison, J.-L., Vola, J.-P., Schmerber, G., Crégut, O., Barre, S., Pourroy, G., Lee, J. H., Jo, W. & Mény, C. Epitaxial thin films of multiferroic $GaFeO_3$ on conducting indium tin oxide (001) buffered yttrium-stabilized zirconia (001) by pulsed laser deposition. *Appl. Phys. Lett.* **91**, 202504 (2007).
14 Sun, Z. H., Zhou, Y. L., Dai, S. Y., Cao, L. Z. & Chen, Z. H. Preparation and properties of $GaFeO_3$ thin films grown at various oxygen pressures by pulsed laser deposition. *Appl. Phys. A* **91**, 97 (2008).
15 Sharma, K., Reddy, V. R., Gupta, A., Choudhary, R. J., Phase, D. M. & Ganesan, V. Study of site-disorder in epitaxial magneto-electric $GaFeO_3$ thin films. *Appl. Phys. Lett.* **102**, 212401 (2013).
16 Saha, R., Shireen, A., Shirodkar, S. N., Waghmare, U. V., Sundaresan, A. & Rao, C. N. R. Multiferroic and magnetoelectric nature of $GaFeO_3$, $AlFeO_3$ and related oxides. *Solid State Commun.* **152**, 1964 (2012).
17 Oh, S. H., Lee, J. H., Shin, R. H., Shin, Y., Meny, C. & Jo, W. Room-temperature polarization switching and antiferromagnetic coupling in epitaxial $(Ga,Fe)_2O_3/SrRuO_3$ heterostructures. *Appl. Phys. Lett.* **106**, 142902 (2015).
18 Mukherjee, S., Roy, A., Auluck, S., Prasad, R., Gupta, R. & Garg, A. Room temperature nanoscale ferroelectricity in magnetoelectric $GaFeO_3$ epitaxial thin films. *Phys. Rev. Lett.* **111**, 087601 (2013).
19 Thomasson, A., Cherifi, S., Roulland, F., Gautier, B., Albertini, D., Meny, C. & Viart, N. Room temperature multiferroicity in $Ga_{0.6}Fe_{1.4}O_3$: Mg thin films. *J. Appl. Phys.* **113**, 214101 (2013).
20 Stoeffler, D. First principles study of the electric polarization and of its switching in the multiferroic $GaFeO_3$ system. *J. Phys. Condens. Matter* **24**, 185502 (2012).
21 Singh, V., Mukherjee, S., Mitra, C., Garg, A. & Gupta, R. Aging and memory effect in magnetoelectric gallium ferrite single crystals. *J. Mag. Mag. Mater.* **375**, 49 (2015).
22 Mishra, S. K., Mittal, R., Singh, R., Zbiri, M., Hansen, T. & Schober, H. Phase stability of multiferroic $GaFeO_3$ up to 1368K from *in-situ* neutron diffraction. *J. Appl. Phys.* **113**, 174102 (2013).
23 Stoeffler, D. First principles study of the spontaneous electric polarization in $Ga_{2-}Fe_xO_3$. *Thin Solid Films* **533**, 93 (2013).
24 Perdew, J. P., Burke, K. & Wang, Y. Generalized gradient approximation for the exchange-correlation hole of a many electron system. *Phys. Rev. B* **54**, 16533 (1996).
25 Vladimir, I. A., Aryasetiawan, F. & Lichtenstein, A. I. First-principles calculations of the electronic structure and spectra of strongly correlated systems: the LDA+U method. *J. Phys. Condens. Matter* **9**, 767 (1997).
26 Blöchl, P. E. Projector augmented-wave method. *Phys. Rev. B* **50**, 17953 (1994).
27 Kresse, G. & Joubert, D. From ultrasoft pseudopotential to the projector augmented-wave method. *Phys. Rev. B* **59**, 1758 (1999).
28 Kresse, G. & Furthmüller, J. Efficient iterative schemes for *ab initio* total-energy calculations using a plane-wave basis set. *Phys. Rev. B* **54**, 11169 (1996).
29 Monkhorst, H. J. & Pack, J. D. Special points for Brillouin-zone integrations. *Phys. Rev. B* **13**, 5188 (1976).
30 Blöchl, P. E., Jepsen, O. & Andersen, O. K. Improved tetrahedron method for Brillouin-zone integrations. *Phys. Rev. B* **49**, 16223 (1994).
31 Abrahams, S. C., Reddy, J. M. & Bernstein, J. L. Crystal structure of piezoelectric ferromagnetic gallium iron oxide. *J. Chem. Phys.* **42**, 3957 (1965).
32 Chang, J., Park, Y. S., Lee, J. W. & Kim, S. K. Layer-by-layer growth and growth-mode transition of $SrRuO_3$ thin films on atomically flat single-terminated $SrTiO_3$ (111) surfaces. *J. Cryst. Growth* **311**, 3771 (2009).

33 Gich, M., Gazquez, J., Roig, A., Crespi, A., Fontcuberta, J., Idrobo, J. C., Pennycook, S. J., Varela, M., Skumryev, V. & Varela, M. Epitaxial stabilization of ε-Fe_2O_3 (001) thin films on $SrTiO_3$ (111). *Appl. Phys. Lett.* **96**, 112508 (2010).
34 Lefevre, C., Shin, R. H., Lee, J. H., Oh, S. H., Roulland, F., Thomasson, A., Autissier, E., Meny, C., Jo, W. & Viart, N. Reduced leakage currents and possible charge carriers tunning in Mg-doped $Ga_{0.6}Fe_{1.4}O_3$ thin films. *Appl. Phys. Lett.* **100**, 262904 (2012).
35 Trassin, M., Viart, N., Versini, G., Barre, S., Pourroy, G., Lee, J., Jo, W., Dumesnil, K., Dufour, C. & Rovert, S. Room temperature ferrimagnetic thin films of the magnetoelectric $Ga_{2-x}Fe_xO_3$. *J. Mater. Chem.* **19**, 8876 (2009).
36 King-Smith, R. D. & Vanderbilt, D. Theory of polarization of crystalline solids. *Phys. Rev. B* **47**, 1651(R) (1993).
37 Vanderbilt, D. & King-Smith, R. D. Electric polarization as a bulk quantity and its relation to surface charge. *Phys. Rev. B* **48**, 4442 (1993).
38 Capillas, C., Tasci, E. S., de la Flor, G., Orobengoa, D., Perez-Mato, J. M. & Aroyo, M. I. A new computer tool at the Bilbao Crystallographic Sever to detect and characterize pseudosymmetry. *Z. Kristallogr.* **226**, 186 (2011).
39 Orobengoa, D., Capillas, C., Aroyo, M. I. & Perez-Mato, J. M. Amplimodes: symmetry-mode analysis on the Bilbao Crystallographic Sever. *J. Appl. Crystallogr.* **42**, 820 (2009).
40 Perez-Mato, J. M., Orobengoa, D. & Aroyo, M. I. Mode crystallography of distorted structures. *Acta Crystallogr. A* **66**, 558 (2010).
41 Song, S., Lee, J. H. & Jang, H. M. Mode coupling between nonpolar and polar phonons as the origin of improper ferroelectricity in hexagonal $LuMnO_3$. *J. Mater. Chem. C* **2**, 4126 (2014).
42 Ravindran, P., Vidya, R., Kjekshus, A., Fjellvåg, H. & Eriksson, O. Theoretical investigation of magnetoelectric behavior in $BiFeO_3$. *Phys. Rev. B* **74**, 224412 (2006).
43 Eyring, H., Lin, S. H. & Lin, S. M. *Basic Chemical Kinetics* Ch. 4 (Wiley, New York, NY, USA, 1980).
44 Jang, H. M., Oak, M., Lee, J., Jeong, Y. K. & Scott, J. F. Softening behavior of the ferroelectric A_1 (TO) phonon near the Curie temperature. *Phys. Rev. B* **80**, 132105 (2009).

Supplementary Information accompanies the paper on the NPG Asia Materials website (http://www.nature.com/am)